A Massive Star's Dying Breaths: Pulsating Red Supergiants and Their Resulting Type IIP Supernovae

Jared A. Goldberg,[1] Lars Bildsten,[1, 2] and Bill Paxton[2]

[1]*Department of Physics, University of California, Santa Barbara, CA 93106, USA*
[2]*Kavli Institute for Theoretical Physics, University of California, Santa Barbara, CA 93106, USA*

ABSTRACT

Massive stars undergo fundamental-mode and first-overtone radial pulsations with periods of 100-1000 days as Red Supergiants (RSGs). At large amplitudes, these pulsations substantially modify the outer envelope's density structure encountered by the outgoing shock wave from the eventual core collapse of these $M > 9M_\odot$ stars. Using Modules for Experiments in Stellar Astrophysics (MESA), we model the effects of fundamental-mode and first-overtone pulsations in the RSG envelopes, and the resulting Type IIP supernovae (SNe) using MESA+STELLA. We find that, in the case of fundamental mode pulsations, SN plateau observables such as the luminosity at day 50, L_{50}, time-integrated shock energy ET, and plateau duration $t_{\rm p}$ are consistent with radial scalings derived considering explosions of non-pulsating stars. Namely, most of the effect of the pulsation is consistent with the behavior expected for a star of a different size at the time of explosion. However, in the case of overtone pulsations, the Lagrangian displacement is not monotonic. Therefore, in such cases, excessively bright or faint SN emission at different times reflects the underdense or overdense structure of the emitting region near the SN photosphere.

Keywords: hydrodynamics radiative transfer stars: massive stars: oscillations supergiants supernovae: general

1. INTRODUCTION

Periodic variability is prevalent in Red Supergiant (RSG) stars, and is interpreted as being a result of radial pulsations (Stothers 1969; Stothers & Leung 1971; Guo & Li 2002). The mechanism driving these pulsations is not fully understood, but they are thought to be driven by a κ mechanism in the hydrogen ionization zone with some uncertain feedback within the convective envelope (Heger et al. 1997; Yoon & Cantiello 2010). Kiss et al. (2006) and Percy & Khatu (2014) identified periods of a few hundred to a few thousand days with varying stellar lightcurve morphology for RSGs in the AAVSO International Database. Such pulsations have also been observed occurring in RSGs within the Small and Large Magellanic Clouds (Feast et al. 1980; Ita et al. 2004; Szczygieł et al. 2010; Yang & Jiang 2011; Yang & Jiang 2012; Yang et al. 2018), M31 and M33 (Soraisam et al. 2018; Ren et al. 2019), M51 (Conroy et al. 2018), M101 (Jurcevic et al. 2000), within HST archival data of NGC 1326A, NGC 1425, and NGC 4548 (Spetsieri et al. 2019), and within the GAIA DR2 RSG sample (Chatys et al. 2019). These works identify these RSG pulsations

as consistent with radial fundamental modes and some first radial overtones.

More luminous RSGs generally exhibit longer periods and higher pulsation amplitudes, with all RSGs in M31 brighter than $M_k \approx -10$ mag ($\log[L/L_\odot] > 4.8$) varying with $\Delta m_R > 0.05$ mag, with R-band variability around $\Delta m_R \approx 0.4$ in some of the more luminous objects (Soraisam et al. 2018). Although it is expected that the metallicity of the host environment might have some small impact on the period-luminosity relationship (Guo & Li 2002), this effect is weak compared to the scatter within the data (see, e.g. Conroy et al. 2018; Ren et al. 2019; Chatys et al. 2019). It is not known whether there is a strong relationship between the host metallicity and pulsation amplitude, but the amplitudes reported for metal-rich M31 are similar to the pulsation amplitudes of RSGs in M33 despite the ≈ 0.25 dex difference in metallicity (Ren et al. 2019). There is, however, a noticeable increase in the number ratio of RSGs pulsating in their fundamental mode versus the first overtone mode with increasing metallicity (Ren et al. 2019).

Multi-epoch studies of Red Supergiants as potential progenitors for direct collapse into black holes are underway (Kochanek et al. 2008), which are ideal for probing the variability of these objects as candidates for core-collapse supernovae (CCSNe) as in Kochanek et al. (2017) and Johnson et al. (2018). So far, the majority of supernovae (SNe) whose progenitors have been

Corresponding author: J. A. Goldberg
goldberg@physics.ucsb.edu

monitored are consistent with no variability, with the exception of the progenitor of the Type IIb SN 2011dh (Kochanek et al. 2017), which was variable in R-band by 0.039 ± 0.006 mags per year (Szczygieł et al. 2012). This is not inconsistent with the near ubiquity of RSG pulsations at high luminosities, as most progenitors observed before undergoing Type II SNe have been on the lower end of the RSG luminosity spectrum (Smartt 2009, 2015), where pulsation amplitudes are likewise generally lower. However, still relatively few such events have been monitored, and there is an open theoretical question about how CCSN lightcurves are influenced by the presence of progenitor pulsations.

Recent work highlights that modeling of lightcurves and photospheric velocities alone is insufficient to extract progenitor characteristics from observed SNe (Dessart & Hillier 2019; Goldberg et al. 2019; Martinez & Bersten 2019). A progenitor radius can provide a crucial constraint, allowing to distinguish between, say, a more compact higher ejecta-mass event with a higher explosion energy, and an event with a larger progenitor radius, lower ejecta mass, and lower explosion energy. This has been done recently by creating matching lightcurve models for SNe with observed progenitor radii (e.g. Martinez & Bersten 2019), fixing a mass-radius relationship by fixing stellar evolution parameters (such as metallicity, mixing length in the H-rich envelope, overshooting, winds) and fitting to a large set of population synthesis lightcurve models (e.g. Eldridge et al. 2019), and in an ensemble fashion by using a prior on the radius of RSGs to extract explosion energies statistically for an existing sample of IIP lightcurves (Murphy et al. 2019). Because, in reality, the progenitor radius could be affected by RSG pulsations, this could lend itself to additional uncertainty in any explosion parameters recovered from SN observations, especially in the case of directly using an observed progenitor radius at an unknown phase relative to the time of explosion.

Observed Type IIP SNe are also often reported to show excess emission before day ≈ 30, often attributed to interaction with the extended environment surrounding the progenitor (e.g. Khazov et al. 2016; Morozova et al. 2017, 2018; Förster et al. 2018; Hosseinzadeh et al. 2018). Because models of early emission depend sensitively on the progenitor density profile (e.g. Nakar & Sari 2010; Sapir et al. 2011; Katz et al. 2012; Sapir & Waxman 2017; Faran et al. 2019), any modification of the outer stellar structure and surrounding environment could translate to distinct changes in the early SN emission (see, e.g., Morozova et al. 2016). For example, the effects of pulsation-driven superwinds (Yoon & Cantiello 2010) on early SN-IIP lightcurves have been directly considered by Moriya et al. (2011, 2017). However, 1D modeling of the extended atmospheres of massive stars is inherently limited, as 1D codes cannot reproduce the detailed 3D structure of the outermost envelope (see

e.g. Chiavassa et al. 2011; Arroyo-Torres et al. 2015; Kravchenko et al. 2019). Therefore, in this work we primarily restrict our discussion to plateau properties after day ≈ 30, at which point the SN emission comes from the modified interior of the star and not the outermost $\approx 0.2 M_\odot$.

In this work, we consider effects of pulsations on the bulk density structure of the stellar envelope and the impact these structural differences have on the resulting Type IIP SNe. In Section 2 we discuss our approach to capturing the effects of radial pulsations on the internal structure of the star using the open-knowledge 1D stellar evolution software instrument Modules for Experiments in Stellar Astrophysics (MESA; Paxton et al. 2011, 2013, 2015, 2018, 2019), and compare our pulsating models to expectations from linear theory. In Section 3 we demonstrate the effects these structural changes have on the resulting SN lightcurves. We show the luminosity at day 50 (L_{50}), time-integrated shock energy (ET), and plateau duration ($t_{\rm p}$) for SNe of progenitors pulsating in their fundamental mode scale simply with the progenitor radius at the moment of explosion as given by Popov (1993); Kasen & Woosley (2009); Nakar et al. (2016); Goldberg et al. (2019) and others. Furthermore, we show that for pulsations where the displacement is not monotonic, such as the first overtone, SN emission from different regions within the ejecta is influenced by the differing structure.

2. MODELING RADIAL PULSATIONS

We construct our fiducial model of a CCSN progenitor with MESA revision 11701. We choose a nonrotating, solar-metallicity ($Z = 0.02$) model of $18 M_\odot$ at ZAMS, with a convective efficiency of $\alpha_{\rm MLT} = 3.0$ in the Hydrogen-rich envelope. We use modest convective overshooting parameters $f_{\rm ov} = 0.01$ and $f_{0,\rm ov} = 0.004$, and winds following MESA's 'Dutch' prescription with efficiency $\eta_{\rm wind} = 0.4$ (Glebbeek et al. 2009; Vink et al. 2001; Nugis & Lamers 2000). After the end of core carbon burning, identified when the central fraction of ^{12}C falls below 10^{-6}, we introduce a maximum timestep of 10^{-3} years. This is to ensure that the model remains numerically converged, as well as to ensure that we resolve changes its structure when causing it to pulsate on a timescale of hundreds of days. Other inputs are determined following the `25M_pre_ms_to_core_collapse` case of the MESA test suite. At the time of core-collapse, 1715 days after the end of core Carbon burning, the unperturbed model has a total mass of $M = 16.3 M_\odot$, a radius of $R = 880 R_\odot$, and a luminosity of $L = 1.56 \times 10^5 L_\odot$.

After evolving the model through the end of core carbon burning, we use the pulsation instrument GYRE (Townsend & Teitler 2013) to identify the periods and radial displacement eigenfunctions for the first 3 radial ($l = 0$) modes. We recover a fundamental pulsation period of 534 days, a first overtone period of 240 days,
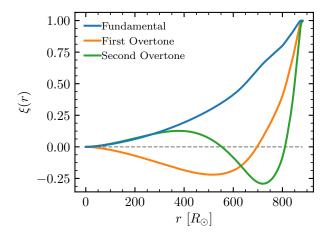
Figure 1. Normalized radial displacement eigenfunctions for our fiducial stellar model at core Carbon depletion.

and a second overtone period of 154 days. The radial displacement eigenfunction $\xi(r)$ for the fundamental mode, and the first and second overtones, normalized to $\max(\xi(r)) = 1$, are shown in Figure 1.

To model the effects of pulsation on the density structure of the envelope, we inject the fundamental eigenmode as a velocity proportional to the radial displacement given by GYRE. For a zone with radial coordinate r, we set $v(r) = 1.2 \, c_{\rm s,surf} \, \xi(r)$, where $c_{\rm s,surf}$ is the sound speed at the surface of the unperturbed model and $\xi(r)$ is normalized to be 1 at its maximum value. The resulting pulsation causes significant variation in the radius, from 760 - 1100 $R_\odot$ over the course of a few pulsations. This amplitude was chosen to resemble the 0.3-0.4 mag amplitudes seen by Soraisam et al. (2018). We do not claim that the growth in the pulsations is being modeled correctly; rather, we are only interested in the effects of realistically large pulsations on the SN properties. In order to achieve core collapse at different phases of the pulsation, we inject this velocity eigenfunction starting at increments of 36.5 days up to 474.5 days after core carbon depletion and allow the model to ring as it evolves to core collapse, as shown in Figure 2. For the fundamental mode, the recovered average peak-to-peak period is 535 days, and trough-to-trough period is 550 days, as the pulsation becomes increasingly nonlinear, especially near the minimum radius. However, both are close to the 534 day period expected of a small amplitude pulsation.

The process of causing our models to pulsate with the first radial harmonic is nearly identical to that described above. However, since the overtone pulsation period of 240 days is approximately half that of the fundamental mode, and there is a node in the radial displacement eigenfunction such that the surface displacement is only caused by oscillation in the outer envelope, the radial pulsation amplitude is comparatively small for a given injected velocity amplitude. Figure 3
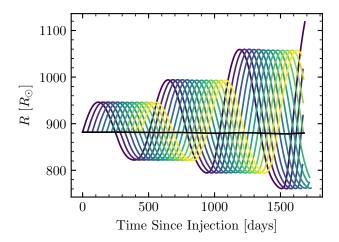

Figure 2. Stellar radius as a function of time, after injecting the velocity eigenfunction of the fundamental radial mode. The left-most point on each curve corresponds to the time of injection relative to the earliest injection, and the right-most point corresponds to the model at the time of core collapse. The black line shows the negligible variation in the stellar radius of the unperturbed model.

shows the overtone pulsation injected with different amplitudes. A fundamental mode is also shown for comparison. The recovered average peak-to-peak and trough-to-trough periods are 236 days and 241 days, respectively, taken over the first 4 pulsation cycles. Particularly for larger amplitude pulsations, the fundamental mode grows in the overtone-injected models, causing modulation on longer timescales than the overtone period. This effect gets stronger with increasing initial pulsation amplitude, making it very difficult to create a model which rings with a "pure" overtone and has a sizeable pulsation amplitude.

2.1. Analytic Expectations in the Linear Regime

For a small perturbation, we can express the radius of that element as $\vec{r} = \vec{r}_0 + \vec{\xi}$, where $\vec{r}_0$ is the unperturbed radius and $\vec{\xi}$ is the Lagrangian displacement. For a radial oscillation with $\vec{\xi} = \xi e^{i\omega t} \hat{r}$, where ω is the frequency of oscillation, the velocity of that fluid element is $\vec{v} = i\omega\vec{\xi}$. By continuity, the density of the fluid element changes as

$$\frac{d\rho}{dt} + \rho\vec{\nabla} \cdot \vec{v} = 0, \tag{1}$$

where d/dt represents the Lagrangian time derivative $d/dt = \partial/\partial t + \vec{v} \cdot \vec{\nabla}$. Equation (1) yields the Lagrangian density perturbation $\Delta\rho$,

$$\Delta\rho = -\rho_0 \vec{\nabla} \cdot \vec{\xi} = -\rho_0 \frac{1}{r^2}\frac{d}{dr}r^2\xi. \tag{2}$$

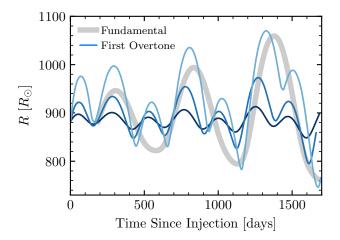In order to check the agreement between our pulsating model and the expectations from linear theory, we save

Figure 3. Stellar radius as a function of time in our models injected with first overtone velocity eigenfunctions. The injected initial velocity amplitudes shown here are $A = 0.69$ (dark blue), 1.71 (average blue), and 3.42 (light blue), for velocities injected of the form $v(r) = A\,c_{\rm s,surf}\,\xi(r)$ where ξ is the displacement eigenfunction for the first overtone. A fundamental mode pulsation is also shown, with its starting point chosen to visually resemble the modulation seen in the overtone models.

Figure 4. Comparison of linear theory for the Lagrangian density perturbation (black lines) with differences in the model density profiles from the density profile of the unperturbed starting model (colored lines) for fundamental mode pulsations (solid) and first overtone pulsations (dashed).

the density profile at the maximum and minimum radius for fundamental mode and overtone pulsations. Figure 4 shows the agreement between our models and Equation (2). Here we normalize ξ to match the displacement in the pulsating model at the mass coordinate corresponding to $300R_\odot$ in the unperturbed model, at an overhead mass of $5.7M_\odot$. This location was chosen because it corresponds to roughly half of the envelope mass and half of the stellar radius in log-space. The surface is most severely affected by nonlinearities, and this work primarily explores effects on the bulk of the material. We also choose to display the overtone profiles at the first maximum (1/4 period after injecting the velocity eigenfunction) and the second minimum (7/4 period after injection) of the model with an injected velocity of $v(r) = 1.71\,c_{\rm s,surf}\,\xi(r)$, as these times are most consistent with being "pure" overtones. The agreement is very good in the interior of the star. Deviations from linear theory occur primarily near the surface, where nonlinearities due to nearly sonic motion cause a larger impact.

3. EXPLODING PULSATING MODELS

At the time of explosion, the density profiles in the envelope vary significantly for different pulsation phases. This can be seen in Figure 5, which shows density profiles in the envelope at core-collapse for the fundamental-mode models as a function of radius (left panel). Additionally, Figure 5 shows a comparison between Lagrangian density profiles of the unperturbed model, a fundamental mode pulsation near max-
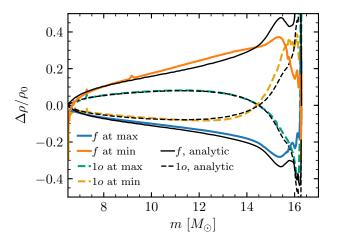
imum, and a large-amplitude overtone near maximum (right panel). In order to achieve a large-amplitude overtone pulsations, we inject a velocity profile with $v(r) = 5.48\,c_{\rm s,surf}\,\xi(r)$, where ξ is the displacement for the first overtone, approximately quarter-period before core-collapse, 1533 days after core C depletion, so that it is approaching its first maximum at the time of explosion. To produce a fundamental mode pulsator with the same stellar radius and similar phase, we inject a velocity profile $v(r) = 2.86\,c_{\rm s,surf}\,\xi(r)$ approximately a quarter-period before core-collapse, 1460 days after core C depletion. Our models show significant diversity in their density profiles, particularly near the surface. Moreover, the overtone pulsation at maximum phase is denser in the interior of the star compared to the unperturbed model, but less dense near the surface, whereas the fundamental mode near maximum is less dense everywhere.

We explode our models at different radii. At a central temperature of $\log(T_c/{\rm K}) = 9.9$, we instantaneously zero out the velocity profile to "freeze in" the density structure of the envelope, since the time to shock breakout (≈ 2 days) is much shorter than the pulsation period, and since the kinetic energy associated with the pulsation is orders of magnitude below the total binding energy of the star. This also helps quell artificial velocity fluctuations which begin to arise in the core around the time of core Si burning. We then continue to evolve the model until core infall. At that point, we excise the core, as described in section 6.1 of Paxton et al. (2018) (hereafter MESA IV). Because each model is evolved independently after core C burning, there is some small variation in the excised mass, ranging from 1.6 to $1.74M_\odot$, leading to ejecta masses of $M_{\rm ej} = 14.54$ to
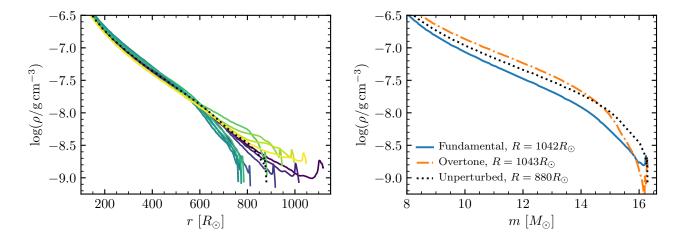
Figure 5. Left: Density profiles in the envelope of our pulsating models just before core collapse, where color corresponds to time the pulsation was injected as in Figure 2. Right: Lagrangian density profiles at core-collapse for large-amplitude pulsations approaching maximum displacement, where the velocity eigenfunctions were injected just 1/4 phase before core-collapse to preserve the purity of the modes. In both panels, the dotted black line shows the unperturbed model.

$14.68 M_\odot$. The unperturbed model has an excised mass of $1.73 M_\odot$. We allow the new inner boundary to infall until it reaches an inner radius of 500 km. We then halt the infall, and inject energy in the innermost 0.1 $M_\odot$ of the star for 10^{-4} seconds, until each model reaches a total energy of 10^{51} ergs.

We proceed by modeling the evolution of the shock including Duffell RTI (Duffell 2016), and hand off the ejecta model at shock breakout to the 1D radiation-hydrodynamics software STELLA (Blinnikov et al. 1998, 2000, 2006; Baklanov et al. 2005) as described in MESA IV. The time to shock breakout is 2 days for the unperturbed model, and varies from 1.7 days for our smallest-radius model to 2.5 days for our largest-radius model. At this explosion energy, there is negligible additional fallback, which we evaluate using the fallback scheme described in Appendix A of Goldberg et al. (2019) with an additional velocity cut of 500 km s^{-1} at handoff to STELLA. We then rescale the distribution of ^{56}Ni to match a total mass of 0.06 $M_\odot$, which is typical of observed events and roughly matches the Ni masses observed in SNe with L_{50} equal to that of the unperturbed model via the $L_{50} - M_{\rm Ni}$ relations from Pejcha & Prieto (2015) and Müller et al. (2017). We use 1600 spatial zones and 40 frequency bins in STELLA, which yields convergence in the bolometric lightcurves for the given ejecta models (see also Figure 30 of MESA IV and the surrounding discussion). While a significant fraction of SNe II-P have excess emission for the first ~ 20 days (e.g. Morozova et al. 2017), and pulsation-driven outbursts have been proposed as one means of mass loss at the end of the lives of RSGs (e.g. Yoon & Cantiello 2010), we do not include any extra material beyond the progenitor photosphere to generate our model lightcurves. In addition, we are focused on the

emission from the bulk of the ejecta, that occurs after day 30.

3.1. Pulsations and Plateau Properties

As discussed in detail by Arnett (1980), Popov (1993), Kasen & Woosley (2009), Sukhbold et al. (2016), Goldberg et al. (2019), and others, the plateau luminosity of a Type IIP SN at day 50, L_{50}, depends on the radius of the progenitor. Popov (1993) gives $L_{50} \propto R^{5/6}$ at fixed ejecta mass $M_{\rm ej}$ and explosion energy $E_{\rm exp}$. From a suite of MESA+STELLA models, Goldberg et al. (2019) recovered a similar scaling, $L_{50} \propto R^{0.76}$. Figure 6 shows lightcurves for the 13 phases of pulsation shown in Figure 2, as well as for the unperturbed model denoted by the black line in Figure 2. As expected from the scalings, the luminosity at day 50 varies by 0.13 dex, or 0.33 mag, with the brighter explosions corresponding to larger radii, with radii ranging from 760-1120$R_\odot$. The slope on the plateau is somewhat steeper in the brighter SNe, such that the variation at early time is greater than closer to the end of the plateau. Additionally, following Goldberg et al. (2019), in the ^{56}Ni-rich limit $M_{\rm Ni} \gtrsim 0.03 M_\odot$, the plateau duration should be approximately independent of the progenitor radius, with some variation for varied distributions of ^{56}Ni and Hydrogen. This can also be seen in our lightcurves in Figure 6, where the recovered plateau durations (using the method of Valenti et al. 2016 as in Goldberg et al. 2019) ranges from 116.8 to 119.5 days with no correlation with progenitor radius. These trends are shown in greater detail in the upper and lower panel of Figure 7, which show good agreement between our models and the scalings.

Figure 5 also shows changes in the outer density profiles and their slopes as a result of these pulsations. These changes do modify the calculated early lightcurves
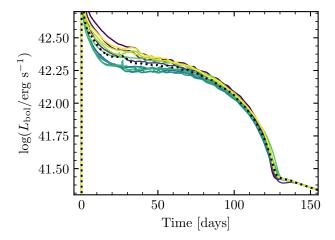
Figure 6. Lightcurves for our fundamental mode pulsator at different phases of pulsation. Color corresponds to time the pulsation was injected, as in Figure 2, and tracks pulsation phase. The dotted black line shows the lightcurve of the unperturbed model.

shown in Figure 6, causing greater luminoisty excesses at early times in the more extended models. In observations, such apparent excesses are often interpreted as evidence for material beyond the normal stellar photosphere. However, because this part of the outer envelope is intrinsically uncertain in 1D models, we are not in a position to make strong claims about whether the variety seen in early lightcurve observations can be explained by pulsations alone.

Additionally, the total energy deposited by the shock is reflected in the observable ET (Nakar et al. 2016; Shussman et al. 2016), defined as the total time-weighted energy radiated away in the SN which was generated by the initial shock and not by ^{56}Ni decay:

$$ET = \int_0^\infty t\,[L_{\rm bol}(t) - Q_{\rm Ni}(t)]\;{\rm d}t, \qquad (3)$$

where t is the time in days since the explosion and

$$Q_{\rm Ni} = \frac{M_{\rm Ni}}{M_\odot}\left(6.45e^{-t/8.8\rm d} + 1.45e^{-t/113\rm d}\right)\times10^{43}\;{\rm erg\;s^{-1}}, \qquad (4)$$

is the ^{56}Ni decay luminosity given in Nadyozhin (1994), which is taken to be equivalent to the instantaneous heating rate of the ejecta assuming complete trapping. ET also scales with the progenitor radius for constant $M_{\rm ej}$ and $E_{\rm exp}$, given as $ET \propto R$ by the analytics and modeling of Nakar et al. (2016); Shussman et al. (2016); Kozyreva et al. (2018), and as $ET \propto R^{0.91}$ recovered from MESA+STELLA models by Goldberg et al. (2019). The middle panel of Figure 7 shows the agreement between ET in our model lightcurves and the scalings. Like with L_{50}, ET as a function of progenitor radius exhibits some scatter, which is not surprising given the
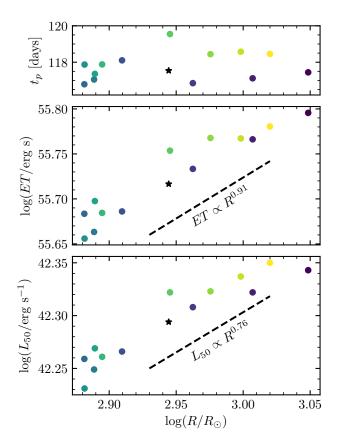

Figure 7. Lightcurve observables versus progenitor radius at the time of explosion for our unperturbed model (black star) and pulsating models (colored points). The plateau duration (upper panel), ET (middle panel), and L_{50} (lower panel) are shown along with scalings from Goldberg et al. (2019). Colors match the colors in Figures 2 and 6.

significant differences in the density profiles especially in the models near pulsation minima at core-collapse, but overall agrees well with the predicted scalings.

3.2. *Comparing Fundamental and Overtone Pulsations*

Although a majority of observed pulsating RSGs are dominated by the fundamental mode, there is evidence for some pulsating with the first overtone (e.g. Kiss et al. 2006; Soraisam et al. 2018; Ren et al. 2019). Because of the radial crossing in the overtone, the progenitor radius used in scaling laws may not be sufficient to predict L_{50}. Typically, the expansion time characterized by the time to shock breakout and the mean density of the SN ejecta are considered in analytics. However, the local radius and density profile of the progenitor at the mass coordinate of the SN photosphere, which is located near the H-recombination front and is defined by the location where the mean optical depth $\tau = 2/3$, must be taken into account. As seen in the left panel of Figure 5, inside the mass coordinate of $\approx 14.5 - 15M_\odot$, which is near the zero-crossing in the radial displace-

ment (see Figure 4), the overtone progenitor model is denser than the unperturbed model, and outside that coordinate it is less dense. On the other hand, the fundamental mode pulsation is less dense everywhere when it is at a positive radial displacement, suggesting that at fixed photospheric mass coordinate in the SN, the star should appear "larger" and therefore the SN would be brighter.

As shown in the upper panel of Figure 8, the evolution of the mass coordinate of the SN photosphere does not change significantly for the pulsating models compared to the unperturbed model. At day 50, the SN photosphere has moved $1.5M_\odot$ into the ejecta for the unperturbed and overtone models, corresponding to a stellar mass coordinate of $14.8M_\odot$, which is near the zero-crossing in the overtone displacement and density perturbation in the progenitor model. This is reflected by the lightcurves shown in the lower panel of Figure 8. The evolution of the photospheric radius (middle panel of Figure 8) and mass coordinate do not differ tremendously on the plateau between the three models, but the lightcurves show a distinct difference. Whereas the progenitor radii for the fundamental and overtone are nearly identical, the overtone explosion at day 50 is fainter by 0.046 dex or 0.115 mags, and in fact much closer in L_{50} to the unperturbed progenitor model than to the fundamental mode. Additionally, the SN from the overtone pulsator is brighter at early times, when the SN emission is coming from what appears to be a more radially extended star with a steeper density profile, and fainter at later times, when the emission appears to be coming from a more compact star.

4. CONCLUSIONS

There is strong observational evidence for variability in large samples of RSGs caused by radial pulsations in their envelopes, typically with periods between a few hundred and a few thousand days (Kiss et al. 2006; Soraisam et al. 2018; Chatys et al. 2019). Since the final stages of burning take place over week-long timescales, much shorter than the pulsation period, the density structure of the envelope can reflect any pulsation phase at the time of explosion. This is significant, as the radius and density structure of a given Type IIP SN progenitor are important in determining the luminosity evolution of its resulting SN.

We consider the effects of pulsations on the stellar envelope and SN emission after core-collapse. We show that SNe of fundamental mode pulsators, which account for the majority of observed pulsating RSGs, behave like "normal" Type IIP SNe from progenitors at different radii. We find that L_{50} and ET scale with the progenitor radius at the time of explosion consistent with the work of Popov (1993); Kasen & Woosley (2009); Nakar et al. (2016); Goldberg et al. (2019) and others, and that the plateau duration remains independent of progenitor radius as expected in the ^{56}Ni−rich regime. The lumi-
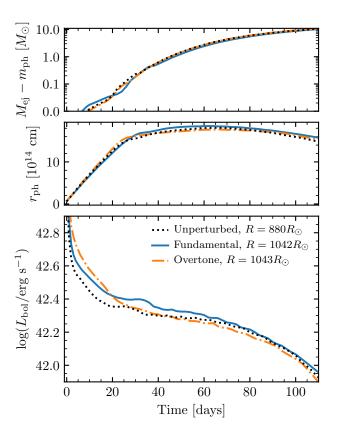

Figure 8. Overhead mass coordinate of the SN photosphere (upper panel), photospheric radius (middle panel), and lightcurves (lower panel) for explosions of large-amplitude fundamental mode and overtone pulsations near maximum, compared to the unperturbed model.

nosity plateau declines more steeply for brighter events between days 30 and 80, which in this study correspond to models with positive radial displacement at the time of core collapse. This is consistent with the observed correlation seen in Type II SNe more broadly between the brightness and steeper plateau decline (e.g. Anderson et al. 2014; Valenti et al. 2016).

Additionally, we show that large-amplitude pulsations in the first overtone yield different lightcurves compared to fundamental-mode pulsations at the same radius. This results from the nonmonotonic overtone density perturbation, which, for an explosion near pulsation maximum, causes the SN to "see" a puffier star at early times, but a more compact star at later times. This yields a supernova which is initially brighter than either the fundamental-mode pulsator at equivalent radius or the unperturbed model at a smaller radius, but fainter once emission is coming from the denser interior. In all cases, the differing stellar radii and density profiles also yield signatures in the calculated early SN emission, but future work aided by a more accurate treatment of the progenitor's extended atmosphere is necessary to make definitive statements and quantitative predictions.

Motivated by the observed oscilllations, we only considered the impact of radial pulsations on the resulting SNe light curves. Non-radial pulsations, if present, would lead to additional phenomena, for example apparent asymmetries during the plateau phase. Existing spectropolarimetric observations (Wang et al. 2001; Leonard & Filippenko 2001; Leonard et al. 2001, 2006; Wang & Wheeler 2008; Kumar et al. 2016; Nagao et al. 2019) sometimes show very low (or undetectable) levels of assymetries during the plateau, with increasing polarization evident in the late time tail attributed to asymmetries deep in the helium core.

Because a fundamental uncertainty in recovered explosion properties from Type IIP SNe stems from the unknown radius at the time of core-collapse, the presence of a pulsation would translate to an additional uncertainty in recovering progenitor properties from SN lightcurves even in conjunction with progenitor detections. Therefore, continued studies of RSG variability will be important in determining the uncertainties within a single progenitor radius detection. Future work is also needed to accurately model the winds and surface layers of massive stars, as well as the density profile of any extended material, all of which are required to effectively model early SN emission and could be affected by these pulsations. Nonetheless, this work highlights the influence of the complete density profile of the progenitor star on the SN emission on the plateau, beyond the initial shock cooling and early spherical phase.

REFERENCES

Anderson, J. P., González-Gaitán, S., Hamuy, M., et al. 2014, ApJ, 786, 67

Arnett, W. D. 1980, ApJ, 237, 541

Arroyo-Torres, B., Wittkowski, M., Chiavassa, A., et al. 2015, A&A, 575, A50

Baklanov, P. V., Blinnikov, S. I., & Pavlyuk, N. N. 2005, Astronomy Letters, 31, 429

Blinnikov, S., Lundqvist, P., Bartunov, O., Nomoto, K., & Iwamoto, K. 2000, ApJ, 532, 1132

Blinnikov, S. I., Eastman, R., Bartunov, O. S., Popolitov, V. A., & Woosley, S. E. 1998, ApJ, 496, 454

Blinnikov, S. I., Röpke, F. K., Sorokina, E. I., et al. 2006, A&A, 453, 229

Chatys, F. W., Bedding, T. R., Murphy, S. J., et al. 2019, MNRAS, 487, 4832

Chiavassa, A., Freytag, B., Masseron, T., & Plez, B. 2011, A&A, 535, A22

Conroy, C., Strader, J., van Dokkum, P., et al. 2018, ApJ, 864, 111

Dessart, L., & Hillier, D. J. 2019, A&A, 625, A9

Duffell, P. C. 2016, ApJ, 821, 76

Eldridge, J. J., Guo, N. Y., Rodrigues, N., Stanway, E. R., & Xiao, L. 2019, arXiv e-prints, arXiv:1908.07762

Faran, T., Goldfriend, T., Nakar, E., & Sari, R. 2019, ApJ, 879, 20

Feast, M. W., Catchpole, R. M., Carter, B. S., & Roberts, G. 1980, MNRAS, 193, 377

Förster, F., Moriya, T. J., Maureira, J. C., et al. 2018, Nature Astronomy, 2, 808

Glebbeek, E., Gaburov, E., de Mink, S. E., Pols, O. R., & Portegies Zwart, S. F. 2009, A&A, 497, 255

Goldberg, J. A., Bildsten, L., & Paxton, B. 2019, ApJ, 879, 3

Guo, J. H., & Li, Y. 2002, ApJ, 565, 559

Heger, A., Jeannin, L., Langer, N., & Baraffe, I. 1997, A&A, 327, 224

Hosseinzadeh, G., Valenti, S., McCully, C., et al. 2018, ApJ, 861, 63

Hunter, J. D. 2007, Computing In Science & Engineering, 9, 90

Ita, Y., Tanabé, T., Matsunaga, N., et al. 2004, MNRAS, 347, 720

Johnson, S. A., Kochanek, C. S., & Adams, S. M. 2018, MNRAS, 480, 1696

Jones, E., Oliphant, T., Peterson, P., et al. 2001–, SciPy: Open source scientific tools for Python

Jurcevic, J. S., Pierce, M. J., & Jacoby, G. H. 2000, MNRAS, 313, 868

Kasen, D., & Woosley, S. E. 2009, ApJ, 703, 2205

Katz, B., Sapir, N., & Waxman, E. 2012, ApJ, 747, 147

Khazov, D., Yaron, O., Gal-Yam, A., et al. 2016, ApJ, 818, 3

Kiss, L. L., Szab, G. M., & Bedding, T. R. 2006, MNRAS, 372, 1721

Kluyver, T., Ragan-Kelley, B., Pérez, F., et al. 2016, in Positioning and Power in Academic Publishing: Players, Agents and Agendas: Proceedings of the 20th International Conference on Electronic Publishing, IOS Press, 87

Kochanek, C. S., Beacom, J. F., Kistler, M. D., et al. 2008, ApJ, 684, 1336

Kochanek, C. S., Fraser, M., Adams, S. M., et al. 2017, MNRAS, 467, 3347

Kozyreva, A., Nakar, E., & Waldman, R. 2018, MNRAS, 483, 1211

Kravchenko, K., Chiavassa, A., Van Eck, S., et al. 2019, arXiv e-prints, arXiv:1910.04657

Kumar, B., Pandey, S. B., Eswaraiah, C., & Kawabata, K. S. 2016, MNRAS, 456, 3157

Leonard, D. C., & Filippenko, A. V. 2001, PASP, 113, 920

Leonard, D. C., Filippenko, A. V., Ardila, D. R., & Brotherton, M. S. 2001, ApJ, 553, 861

Leonard, D. C., Filippenko, A. V., Ganeshalingam, M., et al. 2006, Nature, 440, 505

Martinez, L., & Bersten, M. C. 2019, A&A, 629, A124

Moriya, T., Tominaga, N., Blinnikov, S. I., Baklanov, P. V., & Sorokina, E. I. 2011, MNRAS, 415, 199

Moriya, T. J., Yoon, S.-C., Gräfener, G., & Blinnikov, S. I. 2017, MNRAS, 469, L108

Morozova, V., Piro, A. L., Renzo, M., & Ott, C. D. 2016, ApJ, 829, 109

Morozova, V., Piro, A. L., & Valenti, S. 2017, ApJ, 838, 28

—. 2018, ApJ, 858, 15

Müller, T., Prieto, J. L., Pejcha, O., & Clocchiatti, A. 2017, ApJ, 841, 127

Murphy, J. W., Mabanta, Q., & Dolence, J. C. 2019, MNRAS, 489, 641

Nadyozhin, D. K. 1994, ApJS, 92, 527

Nagao, T., Cikota, A., Patat, F., et al. 2019, MNRAS, 489, L69

Nakar, E., Poznanski, D., & Katz, B. 2016, ApJ, 823, 127

Nakar, E., & Sari, R. 2010, ApJ, 725, 904

Nugis, T., & Lamers, H. J. G. L. M. 2000, A&A, 360, 227

Paxton, B., Bildsten, L., Dotter, A., et al. 2011, ApJS, 192, 3

Paxton, B., Cantiello, M., Arras, P., et al. 2013, ApJS, 208, 4

Paxton, B., Marchant, P., Schwab, J., et al. 2015, ApJS, 220, 15

Paxton, B., Schwab, J., Bauer, E. B., et al. 2018, ApJS, 234, 34

Paxton, B., Smolec, R., Schwab, J., et al. 2019, ApJS, 243, 10

Pejcha, O., & Prieto, J. L. 2015, ApJ, 799, 215

Percy, J. R., & Khatu, V. C. 2014, Journal of the American Association of Variable Star Observers (JAAVSO), 42, 1

Pérez, F., & Granger, B. E. 2007, Computing in Science & Engineering, 9, 21

Popov, D. V. 1993, ApJ, 414, 712

Ren, Y., Jiang, B.-W., Yang, M., & Gao, J. 2019, ApJS, 241, 35

Sapir, N., Katz, B., & Waxman, E. 2011, ApJ, 742, 36

Sapir, N., & Waxman, E. 2017, ApJ, 838, 130

Shussman, T., Nakar, E., Waldman, R., & Katz, B. 2016, arXiv e-prints, arXiv:1602.02774

Smartt, S. J. 2009, ARA&A, 47, 63

—. 2015, Publications of the Astronomical Society of Australia, 32, e016

Soraisam, M. D., Bildsten, L., Drout, M. R., et al. 2018, ApJ, 859, 73

Spetsieri, Z. T., Bonanos, A. Z., Yang, M., Kourniotis, M., & Hatzidimitriou, D. 2019, A&A, 629, A3

Stothers, R. 1969, ApJ, 156, 541

Stothers, R., & Leung, K. C. 1971, A&A, 10, 290

Sukhbold, T., Ertl, T., Woosley, S. E., Brown, J. M., & Janka, H.-T. 2016, ApJ, 821, 38

Szczygieł, D. M., Gerke, J. R., Kochanek, C. S., & Stanek, K. Z. 2012, ApJ, 747, 23

Szczygieł, D. M., Stanek, K. Z., Bonanos, A. Z., et al. 2010, AJ, 140, 14

Townsend, R. H. D., & Teitler, S. A. 2013, MNRAS, 435, 3406

Valenti, S., Howell, D. A., Stritzinger, M. D., et al. 2016, MNRAS, 459, 3939

van der Walt, S., Colbert, S. C., & Varoquaux, G. 2011, Computing in Science Engineering, 13, 22

Vink, J. S., de Koter, A., & Lamers, H. J. G. L. M. 2001, A&A, 369, 574

Wang, L., Howell, D. A., Höflich, P., & Wheeler, J. C. 2001, ApJ, 550, 1030

Wang, L., & Wheeler, J. C. 2008, ARA&A, 46, 433

Wolf, B., & Schwab, J. 2017, wmwolf/py_mesa_reader: Interact with MESA Output, doi:10.5281/zenodo.826958

Yang, M., & Jiang, B. W. 2011, ApJ, 727, 53

Yang, M., & Jiang, B. W. 2012, ApJ, 754, 35

Yang, M., Bonanos, A. Z., Jiang, B.-W., et al. 2018, A&A, 616, A175

Yoon, S.-C., & Cantiello, M. 2010, ApJ, 717, L62